

A contoured gap coaxial plasma gun with injected plasma armature

F. Douglas Witherspoon,^{a)} Andrew Case, Sarah J. Messer, Richard Bomgardner II, Michael W. Phillips,^{b)} Samuel Brockington, and Raymond Elton^{c)}
HyperV Technologies Corp., Chantilly, Virginia 20151, USA

(Received 25 February 2009; accepted 17 July 2009; published online 27 August 2009)

A new coaxial plasma gun is described. The long term objective is to accelerate 100–200 μg of plasma with density above 10^{17} cm^{-3} to greater than 200 km/s with a Mach number above 10. Such high velocity dense plasma jets have a number of potential fusion applications, including plasma refueling, magnetized target fusion, injection of angular momentum into centrifugally confined mirrors, high energy density plasmas, and others. The approach uses symmetric injection of high density plasma into a coaxial electromagnetic accelerator having an annular gap geometry tailored to prevent formation of the blow-by instability. The injected plasma is generated by numerous (currently 32) radially oriented capillary discharges arranged uniformly around the circumference of the angled annular injection region of the accelerator. Magnetohydrodynamic modeling identified electrode profiles that can achieve the desired plasma jet parameters. The experimental hardware is described along with initial experimental results in which approximately 200 μg has been accelerated to 100 km/s in a half-scale prototype gun. Initial observations of 64 merging injector jets in a planar cylindrical testing array are presented. Density and velocity are presently limited by available peak current and injection sources. Steps to increase both the drive current and the injected plasma mass are described for next generation experiments. © 2009 American Institute of Physics. [DOI: [10.1063/1.3202136](https://doi.org/10.1063/1.3202136)]

I. INTRODUCTION

Plasma jets with high density and velocity have a number of important applications in fusion energy and elsewhere, including plasma refueling, disruption mitigation in tokamaks, magnetized target fusion, injection of momentum into centrifugally confined mirrors, plasma thrusters, and high energy density plasmas.

In magnetoinertial fusion (MIF),^{1–4} for example, an imploding material liner is used to compress a magnetized plasma to fusion conditions and to confine the resulting burning plasma inertially to obtain the necessary energy gain. The imploding shell may be solid, liquid, gaseous, or a combination of these states. The presence of the magnetic field in the target plasma suppresses thermal transport to the plasma shell, thus lowering the imploding power needed to compress the target to fusion conditions. This allows the required imploding momentum flux to be generated electromagnetically using off-the-shelf pulsed power technology. Practical schemes for standoff delivery of the imploding momentum flux are required and are open topics for research. One approach for accomplishing this, called plasma jet driven MIF (PJMIF), uses a spherical array of pulsed plasma guns to create a spherically imploding shell of very high velocity, high momentum flux plasma.⁵ This approach requires development of plasma jet accelerators capable of achieving velocities of 50–200 km/s with very precise timing and density profiles, and with high total mass and density. Low- Z plasma

jets would require the higher velocities, whereas some recent calculations^{6–8} have indicated the possibility of using high- Z plasma shells at velocities of only 50–100 km/s.

Thio *et al.*^{5,9} recognized that coaxial railgun accelerators were potentially capable of meeting this challenge, noting that spheromaks and field reversed configurations had already achieved velocities in excess of 200 km/s, albeit with lower densities and total mass. They projected that it would be possible to accelerate 200–400 μg of plasma to ~ 200 km/s in a plasma gun with a length of no more than 1 m and a muzzle diameter of less than 0.2 m, with timing precision of better than 100 ns. Given these parameters, the density of the plasma jets would need to be approximately 10^{17} cm^{-3} .

We describe our work to develop the pulsed plasma gun technology needed for an experimental demonstration of the PJMIF concept and also for the other applications mentioned earlier. The parameters in the previous paragraph were taken as experimental goals. Initial work used existing computational and analytical tools to develop and refine a specific plasma gun concept having a novel tapered coaxial electromagnetic (EM) accelerator profile (originally suggested by Thio¹⁰) and an array of symmetric plasma injectors. The profile is designed to suppress the main barrier to success in coaxial guns, namely, the blow-by instability in which the arc slips past and outruns the bulk of the plasma mass.^{11–13} The first generation half-scale prototype gun is illustrated schematically in Fig. 1.

Our efforts to date have focused mainly on (1) developing various plasma injection systems and ensuring they work reliably with the accelerator section, (2) developing a suite of

^{a)}Electronic mail: witherspoon@hyperv.com.

^{b)}Advanced Energy Systems, Inc., Princeton, NJ 08540.

^{c)}University of Maryland, College Park, MD 20742.

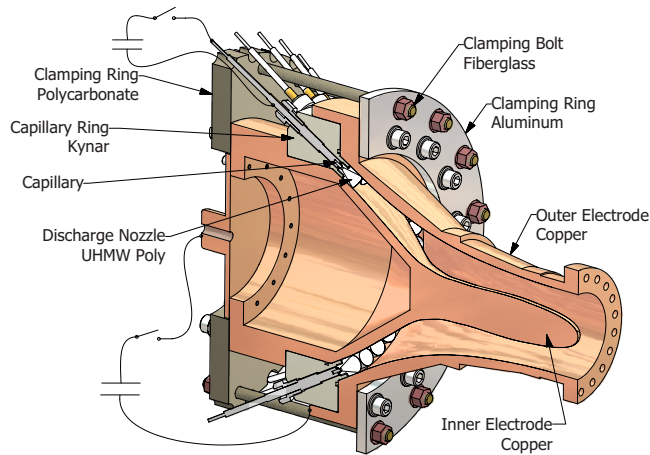


FIG. 1. (Color online) Cutaway view of a first-generation half-scale prototype plasma jet accelerator module which uses tailored electrode profiles to suppress the occurrence of the blow-by instability. Two separate HV circuits power the electrothermal injectors and the main EM accelerator.

plasma and gun diagnostics, (3) performing computational modeling to design and refine the guns, and (4) building a new research facility dedicated to supporting this work. That work has now reached the point where we can concentrate on increasing density and momentum into the desired parameter regime by techniques to be discussed in later sections. Mostly this involves substantial increases in the operating currents (and hence energy) of both the injectors and the main EM accelerator sections, and also by shortening those current pulses in time, and in the near future extending the experimental work to a full-scale gun.

This paper provides an overview description of the basic plasma gun device and initial modeling and experimental results. We first give some background on coaxial accelerators and the motivation for the new methodology we follow which promises to provide a solution to the “blow-by instability” problem in coaxial accelerators. We then describe results from initial numerical simulations using the AFRL MACH2 code^{14,15} to model the plasma macrodynamics. This is followed by a description of the experimental half-scale prototype that was constructed based on those numerical results. We conclude with a description of initial experimental results from that prototype gun and a discussion of the various hardware upgrades currently underway to increase the gun performance into the desired range. A series of follow-on papers currently in preparation will delve more deeply into the both the computational simulations and the experimental/diagnostic investigations.

II. A NEW APPROACH TO COAXIAL PLASMA ACCELERATORS

A. Background

Pulsed coaxial plasma accelerators (or “guns”)^{16,17} have been researched since the 1950s for various applications. Except for the work during the 1950s and 1960s when the research was associated with applications to fusion, most of the research on these accelerators in the past four decades has been associated with applications to space propulsion. During the 1980s and 1990s, plasma accelerators were en-

countered in several other applications, including dense plasma focus and the acceleration of relatively large compact toroids (MARAUDER of the Air Force Research Laboratory,¹⁸ RACE of Lawrence Livermore Laboratory,¹⁹ CTIX of UC-Davis²⁰) for fusion and x-ray generation, and in accelerating solid projectiles to hypervelocity for impact fusion and a variety of defense applications. For space propulsion, these accelerators are called pulsed plasma thrusters (PPTs). Small PPT devices have been successfully fielded on orbiting satellites for station keeping purposes. In these devices, and in the larger plasma guns studied in the 1950s and 1960s, the plasma densities are typically low ($<10^{15}$ cm⁻³) and collisionless. Their development was in part inspired by the 1954 paper of Rosenbluth²¹ which provided the theoretical underpinning for the collisionless acceleration in these guns. Coaxial versions of these guns typically consist of a pair of concentric straight cylindrical conducting pipes serving as the electrodes. Before a shot, the bore of the gun (the region between the electrodes) is first prefilled with the desired propellant gas. By closing a switch that connects a capacitor bank to the electrodes, a current sheet is then initiated near the breech, usually with the help of one or more sparks. This current sheet is essentially a collisionless magnetoplasdynamic (MPD) shock. The collisionless shock then propagates down the bore of the gun. The scheme relies on the shock ionizing the cold prefilled gas, and on the advancing magnetic field sweeping up the resulting ions and electrons. This is known as the snow-plow mode^{16,22} of acceleration. Although there has been some notable success with this approach, culminating in the flying of some devices in practical satellites, the performance of PPTs has been found to be limited by the complexity of the physical phenomena. The complexity arises from the particle kinetic effects coupled to the MPD shocks, and their interactions with neutral particles. An example of the effects that can lead to detrimental performance is the leakage of the particles past the current sheet. These leaked particles lead to low utilization of the propellant, resulting in low mean plasma velocity and efficiency. Further, they are a source of restrike behind the main current sheet, causing further detriment to the performance by drawing drive current from the main current sheet.

B. Dense injected plasma armatures

Consideration of the shortcomings of existing coaxial PPTs led Thio *et al.*²³ to propose an innovative new approach to the plasma dynamics in these accelerators. The main features of their proposed approach were the following.

- (1) No prefill is used. The plasma to be accelerated is preformed and injected impulsively at high density and nearly fully ionized with an initially high electrical conductivity.
- (2) The main body of the plasma is sufficiently collisional that the plasma behaves more like a fluid, in order to suppress undesirable particle kinetic effects.

They essentially laid out a new microphysics approach and basis for plasma accelerators, where microphysics refers

here mainly to localized particle effects. The new approach traded the microphysics problems of conventional PPTs with the engineering challenge of creating the new pulsed plasma feeds (injectors) that would be needed to inject the dense plasmas that meet the requirements of the new microphysics proposed. One of the objectives of our research is to demonstrate the potential of this new microphysics approach to plasma acceleration.

However, having a plausible microphysics approach is only half the challenge. The microphysics also needs to be implemented in a practical macrodynamic scheme, where macrodynamic refers mainly to bulk magnetohydrodynamics (MHD) fluid type behavior and the associated flow geometries. Several challenges remain to be overcome once this highly collisional, no prefill, microphysics approach is adopted. First, the approach requires new plasma injectors to be developed that can deliver the dense plasma that meets the microphysics specifications. Second, in the main plasma accelerator, the notable MHD instabilities and the issues of restrike, skin friction, and electrode ablation and erosion will need to be addressed and overcome.

Thio *et al.*⁹ proposed an accelerator concept as a possible implementation of this new approach. The accelerator consisted of a pair of coaxial electrodes, both electrodes having a gradual conical taper and an EM focusing section much like a plasma focus device. The conical taper induces a small component of radially inward velocity at the muzzle exit which tends to focus the jet for a short distance before collisional effects cause subsequent rebound and expansion further downstream. Whether the focusing provides a net gain in the performance of the jet during its flight to the target remains to be determined, since the induced compressional heating may take back whatever gains were made by focusing.

The acceleration chamber would be thoroughly flushed with helium and evacuated (i.e., no gas prefill). The two electrodes are electrically connected to the two terminals of a capacitor bank or pulse forming network (PFN). Before a shot, the capacitor bank (or PFN) is charged to the desired voltage, which appears simultaneously on the electrodes. The required plasma mass is introduced into the acceleration chamber by a set of extremely low-jitter (<10 ns) pulsed plasma injector feeds arranged annularly near the breech. The plasma is then launched in the form of a plasma “fan” (or “plume”) radially inwards toward the axis of the inner electrode. The plasma fans join to form a dense plasma sheet that closes the external circuit and initiates the main current pulse to accelerate the plasma sheet down the accelerator. A somewhat similar technique was used by Kohno *et al.*²⁴ in a plasma opening switch experiment.

The requisite amount of plasma is injected into the accelerator using pulsed electrothermal capillary discharges with ablative polyethylene walls. Ablative capillaries have been used successfully for large electrothermal guns,²⁵ injectors to high energy railguns,²⁶ plasma thrusters,²⁷ and in experiments involving laser propagation through long plasma channels,^{28–31} to name just a few applications. Ultimately the ablative walls will be replaced with nonablative refractory ceramics, as has been accomplished for pulsed soft x-ray

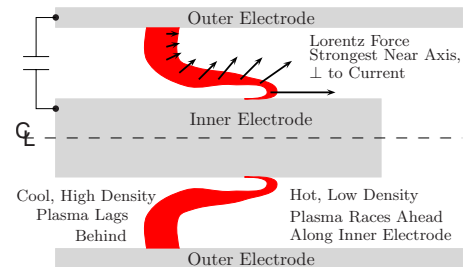


FIG. 2. (Color online) Illustration of blow-by in a straight coax accelerator driven by a HV capacitor. The larger magnetic field and higher current density at smaller radii causes an imbalance in the nominally axially directed Lorentz force, resulting in a faster acceleration of plasma near the inner electrode, which runs away from the bulk of the plasma.

sources^{32–35} and for high energy pulsed thermal spray devices.³⁶ This will allow clean and repetitive operation. The H_2 or D_2 (or other, higher- Z gases) in this case are introduced by other means, which are currently under development at HyperV and will be addressed in future papers.

C. The blow-by instability

Plasma acceleration techniques which depend on Lorentz $\vec{j} \times \vec{B}$ forces are generally susceptible to MHD instabilities that can deteriorate the plasma jet acceleration process significantly, induce restriking and secondary arcs, and even terminate plasma jets. Therefore, it is crucial to understand the MHD instabilities and optimize the design of the accelerator to avoid them in order to achieve the desired plasma jet acceleration. The major instabilities include the blow-by and Rayleigh–Taylor instabilities. The Rayleigh–Taylor instability encompasses filamentation and interchange instabilities.

The main macrodynamic problem in coaxial plasma jet acceleration is the blow-by instability that develops during the acceleration phase. The blow-by instability has its origin in the r^{-2} radial dependence of the magnetic pressure. If the plasma has an initially uniform density and thickness (uniform mass distribution), its acceleration will be higher along the inner electrode than along the outer one. The faster movement along the inner electrode produces a “backward canting” of the current-carrying plasma. The canting current sheet then develops a large axial component which produces a Lorentz force with a radial outward component. This radial acceleration causes a runaway effect in which increasingly more plasma mass is removed from the high velocity region, making the imbalance of the magnetic field pressure against the adverse density profile more severe. As can be seen in Fig. 2, the blow-by instability accelerates a small piece of plasma to a disproportionately high velocity, while leaning most of the plasma mass against the outer electrode where it eventually exits at much lower velocity.

Blow-by was previously investigated by Baker *et al.*^{11,12} More recently, Cassibry *et al.*¹³ performed a detailed computational study of the blow-by instability in straight coax accelerators and found that for straight coax guns, the principal acceleration phase must be limited to no more than about $1 \mu s$ and the electrode radius ratio should be no more than about 2:1. These constraints are too severe to achieve the

goals of this project, but Thio¹⁰ and Cassibry³⁷ also began investigating the possibility of combining pulsed injection along with shaping of the electrode profiles as a means to suppress the blow-by instability and thus achieve higher performance.

D. Coaxial accelerators with tailored electrode geometries

Cassibry³⁷ and Thio¹⁰ had looked at a curved profile coaxial configuration, which showed some promise but was not investigated experimentally. Our approach to addressing the blow-by problem uses a novel shaping of the electrodes originally suggested by Thio.¹⁰ This is basically a further evolution of his straight conical tapered gun mentioned in the last section and the curved profile investigated by Cassibry.³⁷ Our initial modeling effort, described in Sec. IV, focused on analyzing this approach and identifying geometries and parameters which would avoid the blow-by. Although some minor modifications to Thio's¹⁰ original suggestion were found to be necessary, the simulations supported the basic concept.

We thus adopt Thio's¹⁰ microphysics approach that uses highly collisional plasma in a shaped coaxial plasma gun, along with plasma sources that impulsively inject a dense fast-moving preformed plasma armature into a coaxial gun having no initial prefill. Ideally, no external switch would be required, letting the injected plasma itself act as a closing switch, but in practice one may be required.

Assuming an impulsively injected plasma armature, we now consider the physics issues and challenges of controlling the macrodynamics of the plasma slab so that the global characteristics of the plasma acceleration can be achieved.

III. CONTROL OF PLASMA MACRODYNAMICS

A. The injection and transition regions

Figure 3 shows the baseline geometry for the accelerator based on Thio's¹⁰ earlier suggestion. This electrode geometry provides for a breech section (between A and B) that is orthogonal to the gun axis. It was later found to be necessary to change this to an oblique angle, but the following discussion remains essentially unchanged. In this section of the gun, the injected plasma initially flows radially inward toward the gun axis. The initial discharge, initiated by the injected plasma, is axial between the electrodes (and mostly so for the angled injector case), thus forming a fat z -pinch that rapidly accelerates the plasma radially inwards in the region between A and B to supersonic speeds. As the plasma enters the transitional region between B and C, its leading edge is at the outer electrode. Having the leading edge of the plasma at the outer electrode is the preferred inclination for the plasma to counter the blow-by instability. Thio¹⁰ and Cassibry³⁷ call this the "forward canting" of the plasma sheet. Furthermore, the plasma sees a convex curvature at the outer electrode, versus a concave curvature at the inner electrode. The convex curvature produces an expanding fan of the Mach lines (characteristics) for the flow at the outer electrode, giving rise to an expansion of the flow at the outer electrode.

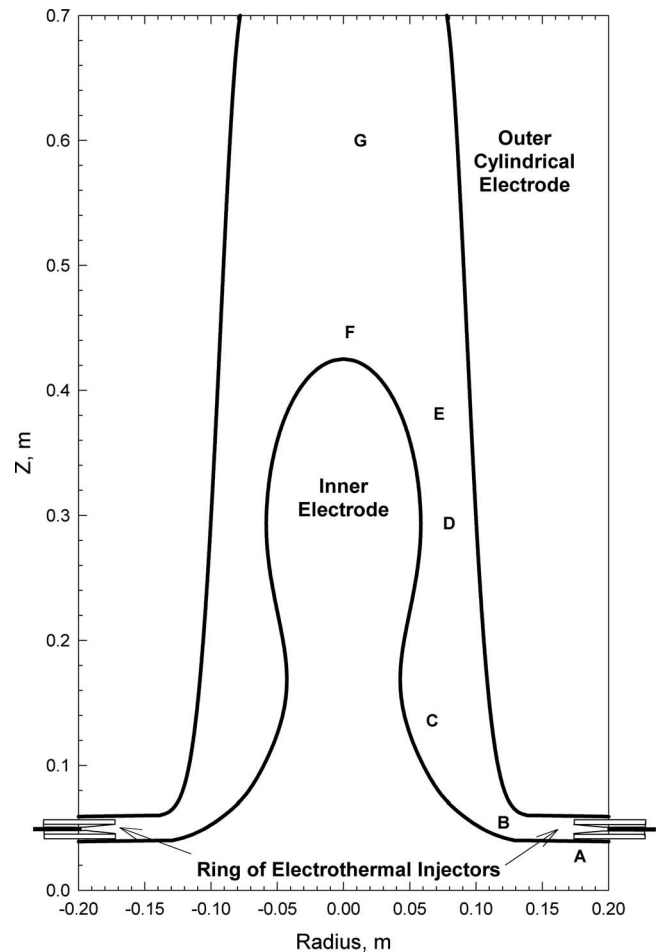


FIG. 3. Baseline plasma jet accelerator geometry for simulations. The right angle turn in this drawing turns out to be too large, and an angle closer to 45° is much better. See Figs. 4 and 5 for examples of simulated plasma flow in this geometry.

The flow expansion helps accelerate the plasma along the outer electrode, reducing the density of the plasma near the outer electrode. On the other hand, the concave curvature relative to the flow at the inner electrode produces convergence of the Mach lines for the flow at the inner electrode between B and C, making the flow bend into itself, giving rise to compression of the flow at the inner electrode. The increased plasma density near the inner electrode tends to reduce the acceleration produced by the greater Lorentz force there. A favorable density profile, monotonic with respect to the magnetic pressure, is thus created by the way the plasma is injected and by the chosen curvatures of the entry and transition regions. These features help to suppress (or at least delay) the occurrence of the blow-by. The electrode profiles are chosen so that the bends produce smooth transitions in the flow, making the compression or expansion as isentropic (shockless) as possible. Our studies showed that the right angle turn is too sharp, while 45° is about right, as discussed later in Sec. IV B.

In the above discussion, we have borrowed fluid dynamics concepts established for steady-flow, even though the flow in our accelerator is unsteady. However, just as is common experience in similar cases, the qualitative descriptions remain essentially correct, while the deviations from the

steady-flow results lie in the quantitative details. The two-dimensional (2D) MHD modeling validated this expectation and the qualitative behavior of the flow as described above is observed in the simulations.

B. The intermediate acceleration stage

The section of the accelerator between C and D is called the intermediate acceleration stage. As the plasma enters this stage, the driving current reaches its peak, and the full Lorentz force is brought to bear on the plasma.

A taper is maintained in the outer electrode to mechanically induce a focusing of the flow toward the axis, the idea being that after the flow exits from the accelerator, the radially inward velocity component of the flow could help counter the thermal expansion of the jet radially, to produce a focusing flow or at least a collimated flow over the required distance.

A gradually decreasing concave curvature is maintained along the inner electrode to continue to reduce the risk of any blow-by instability, seeking to maintain an organized and compact acceleration of the plasma. This is done at the expense of some constriction of the flow and thus some reduction in the acceleration of the plasma through the constriction. This is compensated, however, by the final acceleration stage, in which the concavity in the curvature becomes convex at point D, beyond which the supersonic flow expands along the inner electrode.

C. The final accelerating and focusing stage

The region indicated by points D, E, F, and G represents the final accelerating and focusing stage. The driving current is maintained as close as possible to a flat top equaling its peak value at the point C until the plasma first reaches near the top of the inner electrode (point F). The driving current is ultimately allowed to fall to zero after that as the plasma reaches the point G close to the muzzle.

In addition to the Lorentz acceleration, the supersonic expansion around the inner electrode beyond the point D contributes to the total acceleration of the flow. The convex curvature of the inner electrode also bends the flow toward the axis. Because of the cylindrical geometry, the flow expansion soon ceases and gives in to compression due to convergence of the flow toward the axis. Nevertheless, further acceleration of the flow occurs due to the increasing Lorentz force.

Beyond point D, the plasma at the outer electrode makes gains in the axial position of the plasma at the inner electrode, producing a forward tilting of the current flow. The forward tilting of the current produces a force that accelerates the plasma toward the axis, as well as axially, thus focusing the flow electromagnetically, similar to a dense plasma focus device. The forward tilting of the current increases as the plasma moves toward the point G, producing a conical z -pinch with the tip of the inner electrode as the vertex. The radial pinching of the flow intensifies as the vertex angle of the conical z -pinch decreases, and leads to forward electrothermal acceleration of the plasma axially supported by the intense magnetic pressure due to the z -pinch at

the top of the inner electrode. To further enhance the nearly isentropic compression of the flow, a small concave curvature is provided on the outer electrode in this region. The combination of the EM and electrothermal acceleration propels the plasma forward as a relatively focused jet. The outer electrode has an extended section at the muzzle to provide a guided drift of the accelerated plasma jet to allow it to cool radiatively and convectively in contact with the wall. This lowers the sound speed of the jet and increases its Mach number rapidly as it exits from the muzzle of the accelerator. The high Mach number then maintains the collimation of the focused jet.

IV. ACCELERATOR DESIGN

A series of simulations were performed to find a suitable geometrical configuration and set of parameters that suppresses plasma blow-by and allows at least 100 μg of plasma to be accelerated to 200 km/s. We will briefly summarize the initial modeling results in this section, while deferring to future papers for more detailed analysis. The simulations validated the basic conceptual approach with the restriction that the right angle injection needed to be reduced.

A. The MHD code

To understand the dynamics of contoured coaxial plasma guns and the effect electrode shape has on performance, preliminary design simulations were carried out using the MACH2 code.^{14,15} MACH2 is a 2.5-dimensional single-fluid MHD simulation code. The code follows the nonlinear evolution of density, velocity, and magnetic field, as well as the electron and ion specific internal energies. The code solves equations for mass continuity, fluid momentum, electron, and ion specific internal energies, radiation energy density, and magnetic induction. Quantities are solved on a 2D Cartesian or cylindrical mesh; for the coaxial geometries studied here, a cylindrical mesh was used. The equations are coupled through equation of state (EOS) and transport coefficients. MACH2 features a range of EOS and transport models including table look-up that can utilize the Los Alamos National Laboratory SESAME EOS database.³⁸ Our calculations used the ideal gas EOS, Spitzer resistivity, and Braginskii transport coefficients. The magnetic induction equation can optionally include a Hall effect term in certain geometries, which unfortunately did not include the geometry of interest here. The Hall effect is thought to have an influence on the particle dynamics on the trailing edge of the plasma blob, which may lead, in certain circumstances, to detachment of the current armature. Other than the possibility of detachment, it is not expected to appreciably change the acceleration of the plasma blob. The Hall effect will be left for future study.

A multiblock grid with arbitrary quadrilateral cells and boundary-fitted coordinates is used, which makes possible the simulation of a large variety of complex geometries and boundary conditions. Perfectly conducting walls are assumed on the electrode surfaces. Blocks are connected by overlapping ghost cells. An insulating boundary is assumed at the breech of the gun. For cylindrical geometry, the quantity rB_θ

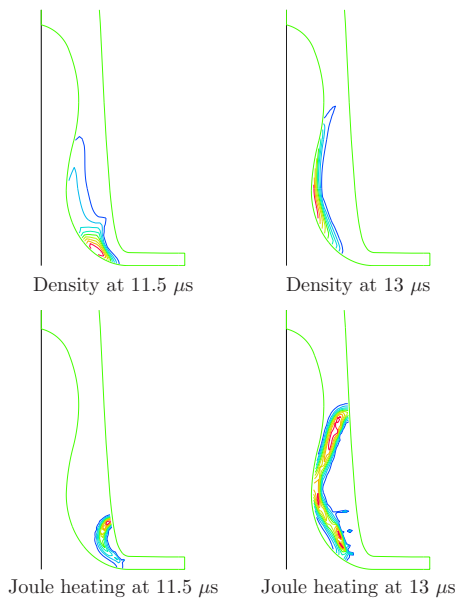


FIG. 4. (Color online) MACH2 density and joule heating contours at 11.5 and 13 μs for baseline Wasp profile run hyperv37. Highest density is the inner red contour, lowest the outer dark blue contour. Velocity plots (not shown) indicate the plasma rapidly accelerating around the corner, leaving a low density pocket there which prevents significant current flow.

is computed on the insulating surface using Ampere's law. These computations used both an LRC circuit model and a prescribed current profile of a shape that can be generated by a PFN. At the beginning of the computation, initial plasma conditions are prescribed on the blocks. For these simulations, an initial annular slug of constant density with an initial velocity directed down the bore of the gun is assumed. This mimics the initial plasma produced by capillary injection. Though these initial conditions may seem highly simplified, the initial density profile was not found to have an appreciable effect on the outcome: during the first microsecond or two, the plasma tends to thermally expand to fill the breech before acceleration gets underway.

B. The wasp profile

Initial simulations used a "Wasp" profile for the center electrode (so-called because of its similarity to a wasp's body) with 90° injection of the plasma, as illustrated earlier in Fig. 3. After running a number of test cases with this configuration, it was observed that this design overcorrects for blow-by. The problem lies with the sharp right angle turn the plasma must make going around the initial corner, where it transitions from the z-pinch into the main accelerator section. This is illustrated in Fig. 4. The momentum of the plasma causes formation of a pocket of very low density plasma just around the corner which rapidly accelerates under both electrothermal and EM forces up along the outer electrode. Meanwhile the main bulk of the plasma continues forward curving around along the inner electrode, generating the very steep density gradient seen in the figure.

The current density peaks in the regions of high conductivity, i.e., where the temperature and charge carrier density are high, as seen in the joule heating contours in Fig. 4. As the plasma accelerates around the curve, it necessarily takes

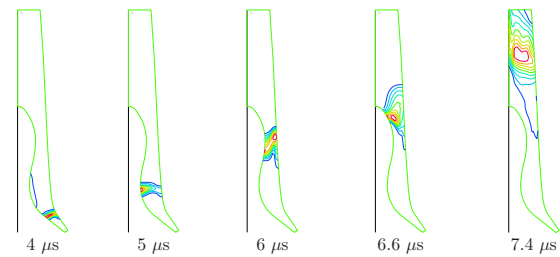


FIG. 5. (Color online) MACH2 kinetic energy density contours for a 200 μg , 200 km/s case for a full-scale "wasp" profile. The total gun length is 75 cm, muzzle diameter is 15 cm, and the diameter at the angled injection point is ~ 33 cm.

the current attachment point on the outer electrode with it. This stretches out the current channel very rapidly. The resulting $\vec{j} \times \vec{B}$ forces then act to further compress the plasma radially inwards against the inner wall. The result is a "blow-by" that occurs on the outside rather than on the inside as in a straight coax.

A set of initial conditions could not be found that circumvents this problem for this specific injection geometry. In this particular configuration, the curvature is excessive and overcorrects, causing the blow-by to occur on the outside. This suggests that the convexity of the outer electrode and the concavity of the inner electrode in the transition from the z-pinch to the main acceleration section needs to be reduced.

C. Systematic tuning of profile curvature

Based on the simulations described above, a new series of simulations were performed to test the original wasp electrode profile, but with an angled injector to provide the correct curvature. The best angle seemed to be around 45° , as was also indicated by another series of simulations using simple circular arc profiles to study armature dynamics. The detailed behavior of the flow from a well performing simulation of the wasp electrode profile is shown in Fig. 5, which shows contours of the kinetic energy density $1/2\rho v^2$. As can be seen from these figures, a compact, well-organized plasma slug is formed early in time. The curvature of the electrode profile continues to maintain a compact plasma as it accelerates up the annular channel, very much as expected theoretically and described in Sec. III above. A number of runs were made with a range of parameters for the initial conditions (injection velocity, density, temperature, and plasma mass). The current density is confined primarily to the compact plasma armature for these best runs. This successful profile, and the range of parameters determining the initial conditions, were later used as the baseline for the design and development of the prototype plasma accelerator.

The plasma is injected at the correct angle to allow the armature to hold together as it accelerates down bore. The $\vec{j} \times \vec{B}$ forces on each end of the armature are balanced so that the extra distance the inner attach point has to travel around the convex curve of the inner electrode (region C in Fig. 3) just allows it to maintain pace with the attach point on the outer electrode. As the armature starts to compress near the throat (region D in Fig. 3), the plasma compresses and a hint of blow-by can be seen near the outer wall, but the compress-

ing plasma prevents it from growing. As the plasma travels through the throat and emerges on the other side it rapidly accelerates toward the axis where it compresses to very high density and then rapidly exits through the muzzle. The bulk flow velocity in the muzzle region of these simulations was about 200 km/s with densities in the range of 10^{16} – 10^{17} cm $^{-3}$ with total mass on the order of 200–400 μ g. The bulk flow velocity is defined as $V_{\text{bulk}} = (2E_{\text{kinetic}}/M_{\text{total}})^{1/2}$. The plasma jet takes on a “smoke-ringlike” structure in most of these simulations with a low density core near the axis, as seen in Fig. 5.

Of particular interest is the potential efficiency of these guns. An estimate is provided by the simulation, which outputs total plasma kinetic energy $E_{\text{kinetic}} = \int 1/2 \rho v^2 d^3x$, energy stored in the magnetic field $E_{\text{magnetic}} = \int \frac{B^2}{2\mu_0} d^3x$, and the energy dissipated as joule heating $E_{\text{joule}} = \int I^2 R dt$. We define the overall gun efficiency as

$$\eta = \frac{E_{\text{kinetic}}}{\frac{1}{2} CV_i^2 - \frac{1}{2} CV_f^2}, \quad (1)$$

where the final capacitor voltage is taken as the peak negative voltage on the capacitor bank at the time of current zero as it rings down. This is essentially equivalent to assuming that all stored magnetic field energy can be recovered in the external circuit. If we further assume an external resistance of 1 m Ω , then the gun efficiency is roughly 59% for the case in Fig. 6(a) and 75% for the case in Fig. 6(b). In all cases we looked at, the total joule heating in the plasma was small compared to the kinetic energy or the magnetic field energy, being typically only 10%–15% of the former, and the simulation gun efficiencies ranged between 35% and 75%. Higher efficiencies are seen for the more massive armatures at lower velocity (such as 50 km/s), as would be expected. This is good news since just these types of plasma jets appear to have promise for PJMIF. These simulations have not included various other effects (such as skin friction drag) which will tend to depress the overall efficiency, and higher external circuit resistance which will need to be kept to 1 or 2 m Ω (skin effect in the rails themselves however is negligible). In any case, efficiencies in the range of 40%–60% appear to be possible and are consistent with reported railgun efficiencies using inductive recapture³⁹ and in pulsed inductive thrusters.⁴⁰ This will require additional work to clarify.

V. PROTOTYPE ACCELERATOR

A cutaway view of the first-generation half-scale prototype plasma accelerator was shown earlier in Fig. 1. The design is based on the wasp profile and MACH2 simulations described earlier, but the half-scale conforms to the physical constraints of installation onto the Maryland Centrifugal eXperiment (MCX) vacuum chamber at the University of Maryland, where it was intended as a driver of rotations in a centrifugally confined mirror plasma.⁴¹ Modeling similar to that of the last section predicted the half-scale gun could accelerate 80–100 μ g of polyethylene plasma to \sim 90 km/s with a 9 μ s current pulse of \sim 190 kA. The experimental

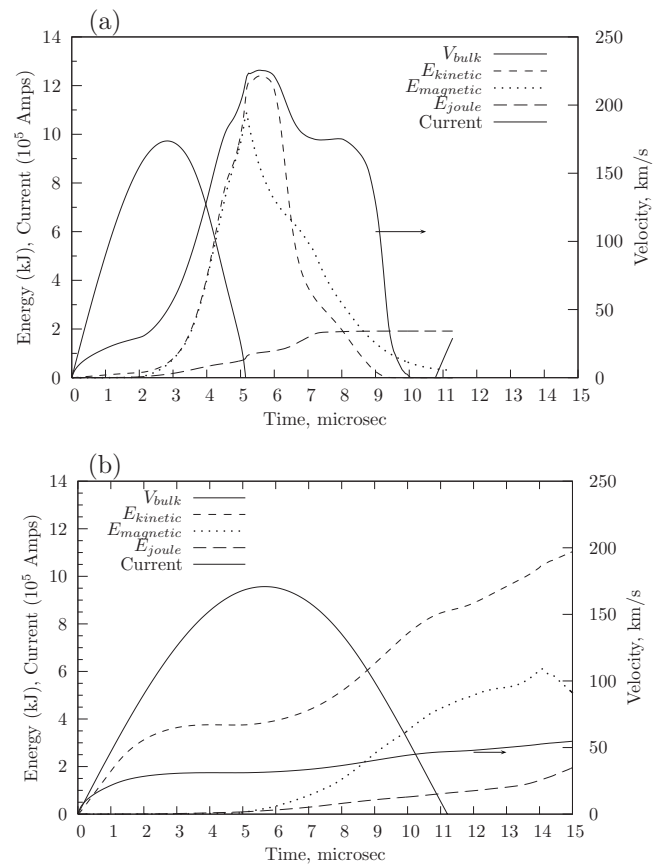


FIG. 6. MACH2 simulations show performance capability of coax gun for (a) low mass (400 μ g) and (b) high mass (\sim 8000 μ g) armatures. Curves peak and then drop off in (a) as plasma leaves computational zone at muzzle exit.

results described below confirm these performance predictions.

The accelerator consists of two main copper alloy electrodes with a ring of 32 equally spaced capillary discharge injector units. The capillaries are mounted in an insulating block of Kynar so that they float electrically with respect to the two main electrodes. The tungsten exit nozzle of each capillary is recessed behind a polyethylene nozzle, which provides a tapered transition to the breech of the main coaxial accelerator. The two main electrodes are held together by two stiff ring structures using 32 insulating fiberglass studs. The Kynar ring also provides high-voltage (HV) insulator standoff between the inner and outer electrodes. Attempts to operate without an external switch have been generally unsuccessful to date. Even at an ambient pressure of 10^{-5} Torr, the structure does not hold off more than about 6 kV after the first shot. It is currently unknown whether this is a fundamental limitation, or whether it could be avoided with a modified design, perhaps using a ceramic insulator instead of plastic. This will be readdressed in the future.

The main electrodes were machined from solid cylindrical “logs” of copper alloy. The inner wall profiles were machined with numerically controlled lathes using profile data from the MHD simulations.

A. Experimental facility

The experimental facility is shown in Fig. 7. The gun is mounted on a support stand and connected to an octagonally

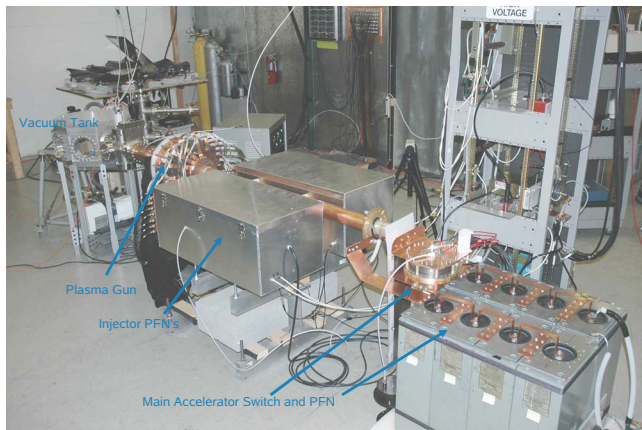


FIG. 7. (Color online) Gun testing facility with the main accelerating PFN in foreground and target vacuum tank in background. The two large boxes in the center contain the capacitors and switches for the 32 capillary injectors.

shaped vacuum chamber (with an inner diameter of 18 in.) through a so-called pinch section (corresponding to region G in Fig. 3). The pinch section consists of a copper tube that carries the final pinching current of the main discharge. Several small ports have been drilled through the wall, which allow insertion of optical and magnetic field probes. A turbopump assembly provides base pressures below 10^{-5} Torr.

We have developed a suite of diagnostics including magnetic and pressure probes as well as time-resolved HeNe interferometry, optical spectroscopy, and fast imaging. There is also an assortment of Rogowski coils and Pearson current monitors to measure the current and voltage supplied to the capillaries and the center electrode. Two cameras were used to obtain both fast and time-integrated signals. These diagnostics and typical results are described in detail in Sec. VI. We have also constructed a fast 16 channel PMT diagnostic based on a Hamamatsu R5900U-00-L16 multichannel photomultiplier array. Time resolution is better than 50 ns, but optical crosstalk between channels creates a practical limit of 4 channels of well-resolved data. Those diagnostics that produce voltage traces on experimental timescales are recorded by 24 Tektronix TDS2000-series oscilloscopes. Each of these four-channel digitizers has a sampling rate up to 1 Gb/s and 100 MHz bandwidth. A screen room shields the oscilloscopes from electrical interference during the HV shots. The oscilloscopes are controlled and read by custom Python-based software.

The 20 kV, 96 μF capacitor bank supplying the main discharge current is typically charged to 18 kV. The PFN is configured as two parallel legs of four 12 μF Maxwell capacitors in each leg as illustrated in Fig. 8. An adjustable ballast resistance of 30–60 m Ω roughly matches the PFN to the discharge in order to reduce ringing (although it is never entirely eliminated). The capillaries draw current from a set of eight 40 kV, 0.15 μF capacitors. Charge and dump operations are controlled with a set of 120 VAC drop hammers. A pair of Titan 40264 sparkgap switches discharges the capillary capacitors. A single Beverly III Associates SG-172CM2 sparkgap switch discharges the main PFN.

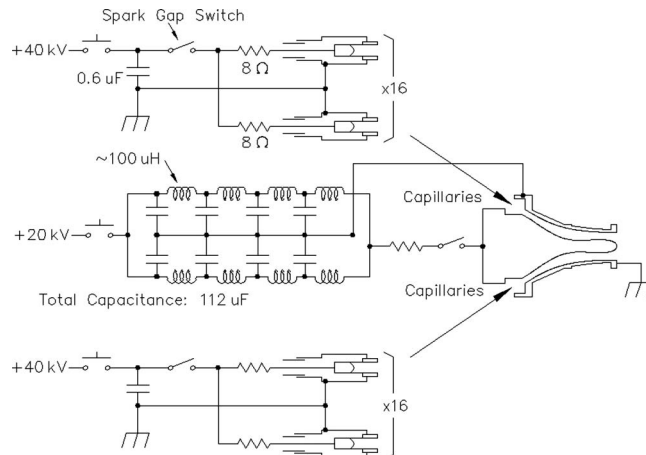


FIG. 8. Schematic of accelerator system showing two separate HV circuits for the capillary injectors and the main accelerator, respectively.

B. Plasma injection

Plasma injection is accomplished using a large number of small capillary discharge units. Each of the capillaries is a HV coaxial unit. The output end of the capillaries provides an axial discharge path across the ablative plastic insulation. A surface discharge across this insulation connects the inner and outer electrodes, heating and vaporizing the polyethylene insulation. The resulting plasma expands to fill the interior tube. Ohmic heating of the plasma combines with magnetic forces to eject a hot, dense plume past the tungsten nozzle. Plumes from neighboring capillaries combine to form a uniform ring of plasma connecting the inner and outer electrodes of the main gun. The electrical energy input to the capillaries must be split between heating, ablating, and ionizing the polyethylene surface. Thermal pressures dominate the resulting plasma. As a result, the injection velocity is near Mach 1, typically 10–14 km/s for these polyethylene plasmas.

Initial designs for the capillary injectors used a series of sealing O-rings and was both expensive and complex to assemble. Later designs moved toward press-fit and glued seals. The components are cheaper, assembly is faster, and both vacuum and HV performance are just as good as for the original design. The center, HV electrode is an off-the-shelf 1/8 in. (3.18 mm) diameter tungsten welding rod. The

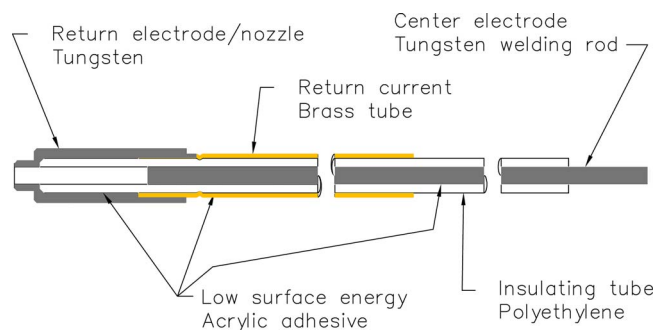


FIG. 9. (Color online) Detailed view of internal structure of capillary used in main accelerator. Except for the tungsten nozzle which requires machining, all components are commercial-off-the-shelf items simply cut to length. Internal vacuum seals are achieved using acrylic adhesives.

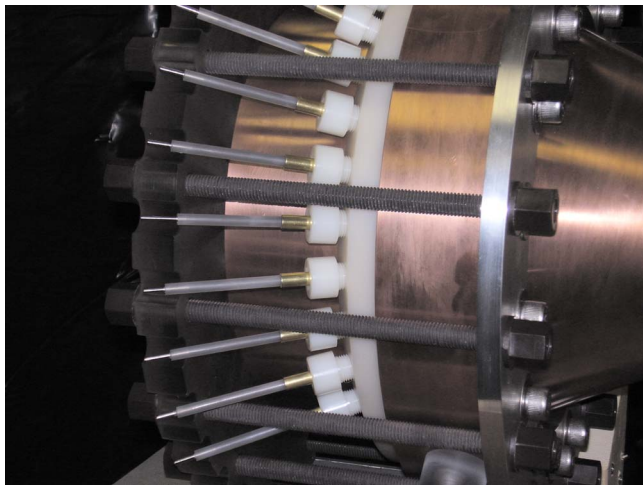


FIG. 10. (Color online) Closeup view of capillary HV connections extending out the back of the gun from their insulating carrier bolts. Current enters through the center tungsten electrode and returns via the coaxial brass tube. An external coaxial braid (not shown) keeps the current coaxial to reduce noise generation in diagnostics and other circuitry. See also Figs. 9 and 11.

grounded outer conductor is a brass cylinder. The nozzle electrode is tungsten. A high density polyethylene tube provides the HV insulation and ablative mass. An assembly drawing of the final design is shown in Fig. 9. The capillaries can be seen protruding from the rear of the accelerator in Fig. 10, with the internal mounting details in the annular breech of the accelerator illustrated in Fig. 11.

Once a capillary establishes a surface discharge, its resistance drops as the increasing capillary current heats the plasma. Initially, this led to the concern that the capillary array would operate unevenly, i.e., the voltage would drop too low to complete the discharge initiation of the remaining capillaries once the first one went. This would result in a highly asymmetric injection into the main gun. Such high asymmetry would accelerate the development of the Rayleigh–Taylor instability and sharply limit gun performance. To avoid this situation, early designs placed a ballast resistor in series with each capillary, but the explicit ballast resistors ultimately turned out to be unnecessary, since the stray (inductive) impedances in the circuit were found to be sufficient to maintain balance.

We have established reliable symmetric operation of 32 capillaries (and 64 in the TwoPi device discussed later) by connecting each capillary to the switch through a single

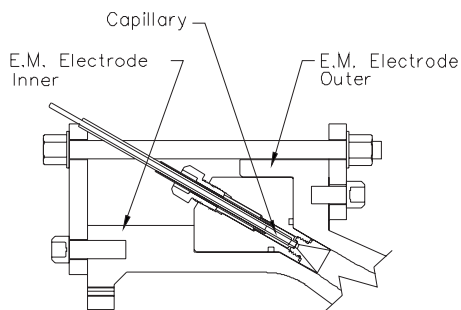


FIG. 11. The capillaries are mounted in a plastic Kynar ring with individual polyethylene nozzles.

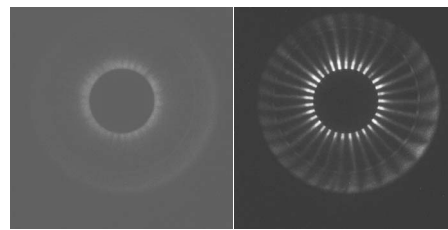


FIG. 12. Left: fast PImax image of capillaries firing. Gate is 25 ns wide triggered at $t=0$. Right: gate of 1 μ s. Capillary discharge fully established. Both images looking back up through the muzzle. Dark central circle is the center electrode.

cable. There are two Titan switches in parallel, each of which controls the current to 16 capillaries. Each Titan switch gates the current from four 0.15 μ F capacitors typically charged to 35 kV. Eliminating the ballast resistors allowed more of the capacitor energy to be used in ablation and heating of the polyethylene, which produced higher density and higher-temperature capillary discharges. The capillaries all fire within about 25 ns, as shown in Fig. 12. Typical capillaries currents are 3–5 kA, with a ~ 1.54 μ s period, and a subsequent $1/e$ decay time of ~ 3.2 μ s.

C. Sparkgap gun

As an alternative to the capillary injector approach, a second approach using sparkgap injectors was also built and tested. This configuration uses a much larger number of small tungsten electrodes mounted with their tips roughly flush with the inside surface of an annular insulator ring at the breech of the gun. This is illustrated in Fig. 13. The external HV circuit is arranged so that the electrode tips alternate in polarity: ground-HV-ground-HV-ground.... Surface arc discharges along the insulator, with alternating current direction, then ablate the local polyethylene surface, ejecting plasma into the gap between the coaxial electrodes. Due to the much larger number of plasma sources, 112 sparkgap electrodes versus 32 capillaries, a higher degree of symmetry in the injected plasma can be achieved. The electrodes consist of off-the-shelf tungsten welding rods with a diameter of 1/16 in. (1.6 mm) by 6 in. (15.2 cm) long. They

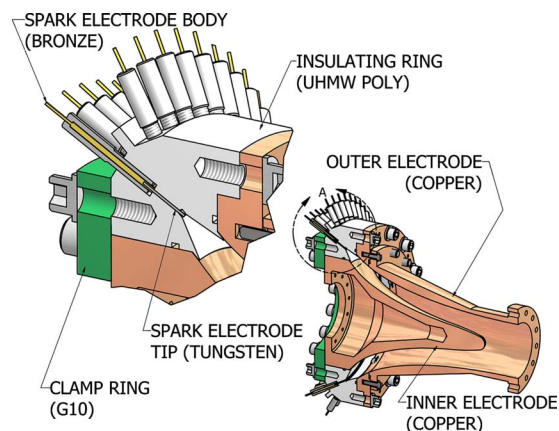


FIG. 13. (Color online) Sparkgap gun configuration with 112 tungsten electrodes and a center electrode with a smooth circular arc profile instead of the “wasp” profile of the first prototype gun shown in Fig. 1.

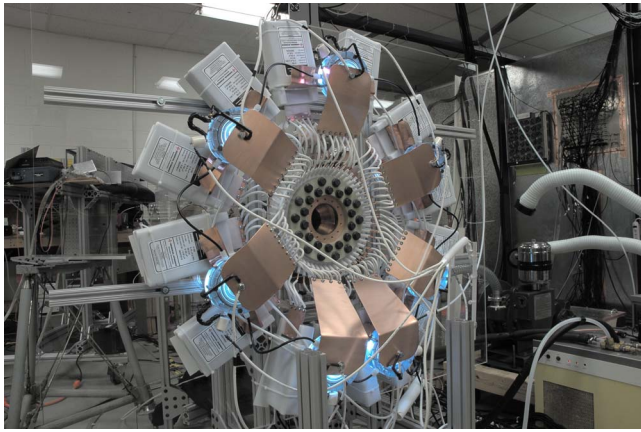


FIG. 14. (Color online) Rear view of sparkgap gun with main bank disconnected to show only the 112 sparkgap injectors firing.

are carefully press-fit into a slightly undersize hole in the polyethylene, forming a tight vacuum seal that allows base pressures into the 10^{-6} Torr range. Figure 14 shows the HV connections surrounding the gun. There are seven switches, each of which connects two $0.15 \mu\text{F}$ capacitors to 16 electrodes. A combined total of almost 0.7 MA is driven through the 112 sparkgaps generating the injected plasma.

D. TwoPi test fixture

The “TwoPi” test fixture was built to allow development testing of large capillary arrays and their associated HV circuitry. The initial version used a disk-shaped vacuum chamber with an inner diameter of 19.5 in. (49.5 cm) and inner height of 2 in. (5.1 cm). 64 radially inward pointing capillaries (essentially identical to those used on the gun) are arranged uniformly around the periphery, as seen in Fig. 15. Large top and bottom acrylic viewing flanges allow optical probing and imaging of the plasma as it emerges from the capillaries and propagates toward the center. Test results from a slightly smaller diameter TwoPi with an upgraded power supply are described later in Sec. VI H.

VI. EXPERIMENTAL RESULTS

We discuss below typical characteristics for the half-scale prototype gun used on MCX. Variations in the ballast resistances, fill pressure, and other machine parameters were observed to shift these numbers. For example, the electron density was found to increase from 4×10^{14} to

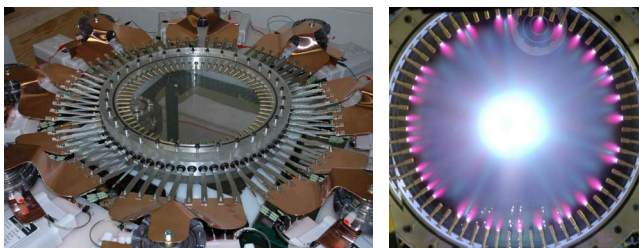


FIG. 15. (Color online) Left: arrangement of the original TwoPi test fixture showing copper bus plates, ballast resistors, capacitors, switches, and vacuum vessel. Right: Nikon open shutter photograph of a test shot in original TwoPi test fixture.

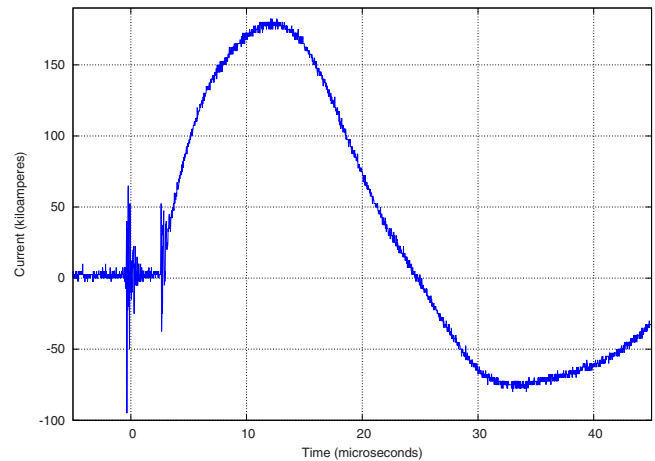


FIG. 16. (Color online) Main accelerating current rings due to impedance mismatch.

$6 \times 10^{14} \text{ cm}^{-3}$ when the ballast resistor was decreased from 8 to 0Ω . For purposes of definiteness and direct comparisons, all measurements quoted below are made with 0Ω ballast resistance on the capillary plasma injectors and a $1 \mu\text{s}$ delay between firing the capillaries and the main PFN. The background pressure is less than 10^{-5} Torr of air (i.e., no separate gas filling).

A. Gun electrical

The main gun’s current and voltage waveforms are routinely measured. A Rogowski coil records peak currents of about 174 kA on each shot. The first half-cycle of the current ring lasts $22.8 \mu\text{s}$, and the reverse current is 44% of the peak current (see Fig. 16). Voltage is obtained by a Pearson monitor measuring current through a $1 \text{ k}\Omega$ resistor across the gun’s breech. The current waveform varies smoothly over the course of the shot, suggesting that any restrikes or filamentation provide only gradual changes to the gun impedance. Additional Rogowski coils measure the current to individual capillaries. These Rogowski coils show 5 kA per capillary.

B. Visible light imaging

A Nikon D70s digital camera routinely gives time-integrated color pictures of the plasma discharge from various angles. These typically show a bright blue-white plasma flowing from the gun muzzle and gradually expanding downstream, as seen in Fig. 17. A pink plasma fills the target chamber, and a dimmer blue plasma rebounds off the back wall of the chamber. The interior of the gun is filled with a bright blue plasma, and there is often evidence for distinct bright-white filaments between the inner and outer electrodes (future work will attempt to determine when and where these occur within the gun). Photographs of the capillary plasma plumes taken without firing the main PFN confirm that all capillaries fire on virtually every shot (Fig. 12).

A fast PImax camera (model 7489-0004) is used to image the gun plasma on submicrosecond time scales. It confirms that the capillaries fire simultaneously within 25 ns. The PImax shows the gun produces a dense bright stream of

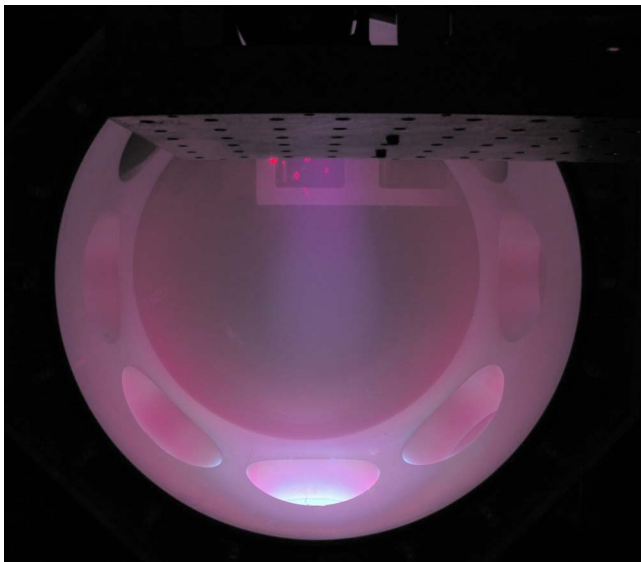


FIG. 17. (Color online) Nikon open shutter photograph of bright jet plume in vacuum tank. One arm of the interferometer and the interferometer probe beam are visible at the top of the image. Plasma jet travels toward the bottom where it stagnates on one of the 8 side port windows.

plasma (Fig. 18). If the background pressure is raised to the vicinity of 1 mTorr, the stream of plasma condenses into a discrete blob.

Photodiodes have been positioned to look across the plasma flow. These measure speeds of the luminous front ranging up to ~ 143 km/s for some gun configurations.

C. Spectrometry

We used a compact Ocean Optics, Inc. survey spectrograph to identify interesting regions in the plasma spectrum, time-integrated over the event. It showed spectra consistent with a 2:1 hydrogen-to-carbon ratio, as expected for the ablative polyethylene capillaries used for plasma injection. Interesting regions identified by the spectrograph were further examined using a 1 m stigmatic Czerny/Turner spectrometer (Acton Model 410) with the PImax camera previously mentioned used for capturing the spectra. It was

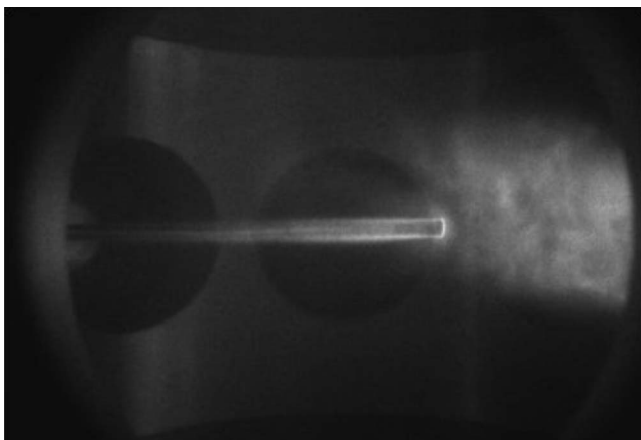


FIG. 18. PIMax image of plasma stream incident on the pressure probe. This image coincides with an increase in the measured pressure. The bright spot at the probe tip and the dim arc upstream of it are reproducible features of the bow shock.

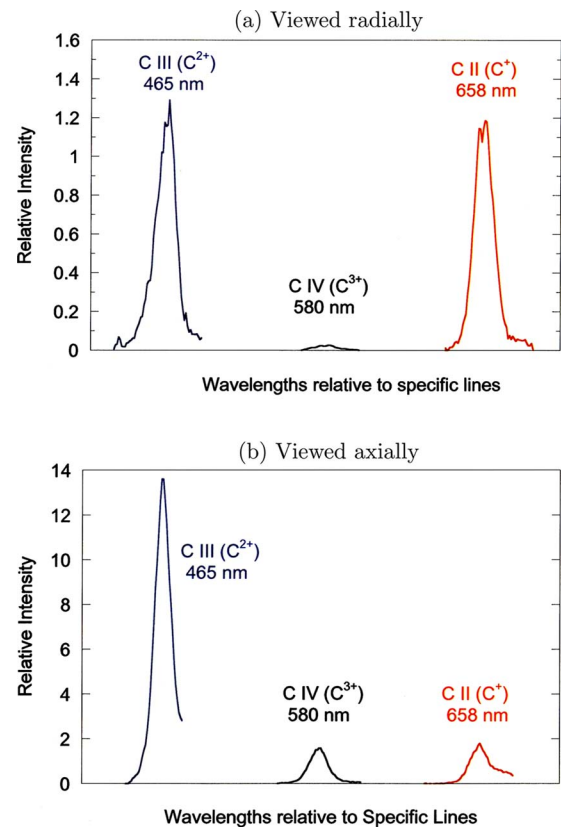


FIG. 19. (Color online) Relative line intensities for carbon ions. (a) Viewed radially from the gun, implying an electron temperature in the blob from ionization balance of $kT_e \sim 4\text{--}5$ eV. (b) Viewed axially inside the gun, implying an electron temperature internal to the gun from ionization balance of $kT_e \sim 5\text{--}6$ eV, higher than in the expanding blob.

coupled to the experiment by two $100\ \mu\text{m}$ diameter fiberoptic cables aligned along the entrance slit, thus permitting two simultaneous views of the plasma, e.g., axial and radial. The monochromator was equipped with an 1800 grooves/mm grating for a nominal reciprocal linear dispersion at the exit of $0.5\ \text{nm/mm}$. With a pixel size of $0.011\ \text{mm}$ at the charge coupled device (CCD), this dispersion translates to nominally $0.006\ \text{nm/pixel}$ at the detector output. Hence, a detector coverage of 1024 pixels yields a wavelength span of nominally $6.1\ \text{nm}$ at any one wavelength setting. A spectral resolution of 6 pixels (as determined from spectral lamps) results both from the selection of a $50\ \mu\text{m}$ wide entrance slit and from a somewhat larger pixel size ($16\ \mu\text{m}$) for the image intensifier in front of the CCD.

Spectral lines from neutral hydrogen (Balmer series), as well as carbon atoms up to 3 times ionized (C IV spectra) are recorded and analyzed. The intensity ratio of carbon-ion lines yields an electron temperature in the slug as high as $4\text{--}5$ eV, and $5\text{--}6$ eV in the gun itself when viewed axially. These are based on calculations⁴² of ionization balance (see Fig. 19). Interestingly, neutral C I emission is *not* observed, implying an electron temperature greater than ~ 2 eV.

Doppler shift measurements along the axis of the gun indicate a mean C^+ velocity of $80\text{--}90$ km/s, with a lesser component exceeding 100 km/s (see Fig. 20). There is also a somewhat stationary component (arising either at the gun or at the output window) that at times distinctly shows a portion

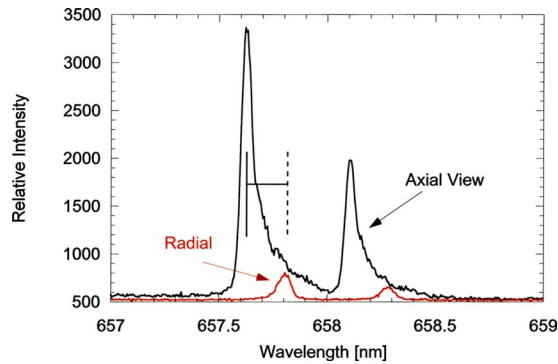


FIG. 20. (Color online) Velocity for C^+ ions from the Doppler shift in two C II spectral lines viewed along the axis compared to the unshifted radial view. A shift in 0.18 nm here is equivalent to a velocity of ~ 82 km/s.

moving with a velocity of ~ 12 km/s. For the same shots on which photodiodes measured 143 km/s, the Doppler shift in the fastest H- α component corresponds to a speed of 147 km/s (see Sec. VI B).

The widths of hydrogen Balmer- β and - γ lines observed radially indicate⁴³ an electron density $\sim 5 \times 10^{14}$ cm⁻³, averaged across the column (Fig. 21). This is likely a slight overestimate of the electron density after correcting for a small Doppler broadening contribution. Other configurations have shown higher electron densities, ranging up to $\sim 5 \times 10^{15}$ cm⁻³, depending primarily on the fill pressure (see also Secs. VI E and VI F).

D. Ballistic pendulum tests

Initial measurements of the plasma slug momentum were made using a fast camera and a low mass ballistic pendulum consisting of a plastic Petri dish suspended by a tungsten wire. A PImax fast camera recorded the image at multiple time delays. The pendulum mass and maximum vertical rise give the change in its potential energy ($\Delta E_p = m_{\text{dish}} g \Delta h$). From this we calculated the pendulum initial kinetic energy [$\Delta(E_K + E_p) = 0$] and momentum ($p_{\text{dish}} = \sqrt{2m_{\text{dish}} E_K}$). If all this momentum is transferred from the plasma, the plasma momentum p_{slug} is not less than the initial momentum of the dish, p_{dish} . (We equate the momenta of the dish and plasma slug rather than using the kinetic ener-

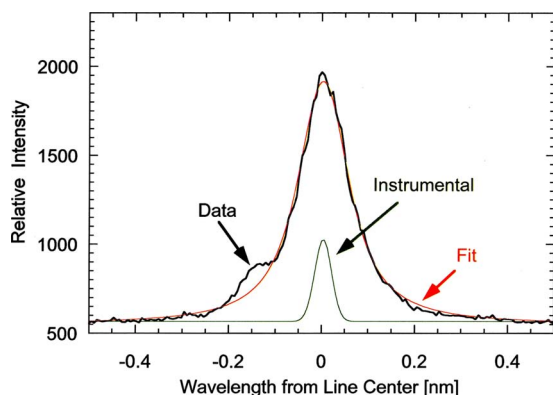


FIG. 21. (Color online) Stark broadened H- β Balmer line of neutral hydrogen with a Lorentzian fit at an electron density of $N_e = 5 \times 10^{14}$ cm⁻³. The lack of a central dip is attributed to integration along the radial line of sight.

gies. This accounts for the likelihood of an inelastic collision involving heating and radiation.) The chamber was evacuated, so the momentum lost to drag is negligible. In addition, the dish is wider and much more massive than the plasma, so the amount it moves during the impact event is tiny, and it blocks the entire plasma throughout impact. We confirmed that this momentum transfer results from the main accelerated plasma jet by firing the injector capillaries without the main gun. In this case, no pendulum motion was detected. Typical direct measurements are: $m_{\text{dish}} = 28.9$ g, 21° displacement, and $v_{\text{slug}} = 90$ km/s (from spectroscopy, Sec. VI C). From the measured angular displacement, the dish undergoes a vertical displacement of 9.7 mm. The measurements imply a plasma momentum of 13 g m/s and a mass of 140 μg . Raising the background pressure to ~ 1 m Torr has been observed to lower the momentum to 11 g m/s. The pendulum measures a somewhat higher total momentum (and mass) than the value estimated from other diagnostics (see Secs. VI C and VI E). This is probably due to a “rocket” effect of material ablated from the dish surface by the plasma.

E. Interferometry

The HyperV interferometry system is a 632 nm HeNe laser quadrature heterodyne interferometer using a single pass through an acousto-optic modulator at 110 MHz which serves as both the modulation source for the reference beam and the beam splitter. The unmodulated scene beam makes two passes through the plasma before recombining with the modulated reference beam on a polarizing beam splitter. The scene beam makes two passes through a quarter wave plate, rotating the direction of polarization through 90° so that the scene and reference beams have orthogonal polarization when recombined on the beamsplitter. The combined beam is passed through a polarizer at 45° to the polarization direction of the beams, projecting the sense of polarization onto the same axis. Detection is via a fiber coupled reverse biased PIN diode, and the signal is demodulated using a quadrature heterodyne detection circuit. This arrangement measures the line-integrated electron density across the output plasma blob 17 cm downstream from the muzzle. If we estimate the path length from PImax photographs (10 cm at the position of the interferometer), we find a typical density is 5×10^{14} cm⁻³. This density is comparable to that obtained by Stark broadening, as described above. The 90 km/s speed of the plasma and the observed duration give an estimated plasma slug length of about 1 m. A 10 cm diameter column 1 m in length with this electron density and an average ion mass of 5 amu will have a mass of about 33 μg . (Compare measurements in Secs. VI C, VI D, and VI F.)

Optical spectroscopy (Sec. VI C) on the sparkgap gun has routinely measured Doppler shift velocities of 100 km/s for carbon and hydrogen lines. The HeNe interferometer shows that the plasma is produced in multiple pulses (due to current ringing). To obtain a mass estimate, we assume an average ion mass of 5.5 amu per free electron, and use the 100 km/s speed to convert the time history into a spatial profile. With these assumptions, integration of the first pulse alone gives a mass of 200 μg from the interferometer traces.

F. Pressure probe

We have constructed a fast pressure probe incorporating a commercial piezoelectric pressure sensor from PCB Piezotronics (Model 113A21, used in combination with a Model 480D06 bias and amplifier unit.) The stainless-steel sensor is epoxied inside the end of a 9.5 mm outer-diameter quartz tube and is protected from the plasma by a 0.5 mm thick polished quartz disk. Shock tube calibrations indicate the probe has a nominal $0.8 \mu\text{s}$ rise time, although there is an acoustic resonance near 160 kHz. For pressures lasting longer than $2 \mu\text{s}$, the probe generates a signal of about 2.3 mV/kPa.

When this probe is aligned for head-on collision with the plasma slug, it measures an increase in pressure coincident with the arrival of the luminous plasma stream described in Sec. VI B. At a distance of 15 cm downstream from the muzzle, this signal shows a flattop pulse of ~ 150 kPa and has a full-width, half-maximum duration near $10 \mu\text{s}$. This is approximately the adiabatic stagnation pressure of the plasma flow. We combine this pressure with the 90 km/s velocity from spectroscopy, the electron density from interferometry and Stark widths, and with estimates of $Z=1$, $T=3$ eV, and $\gamma=5/3$ to estimate the mass per ion as 5.8×10^{-27} kg = 3.5 amu. We can estimate the plasma momentum density by multiplying this mass by the density and velocity from optical diagnostics. This gives $0.26 \text{ kg m}^{-2} \text{ s}^{-1}$. If we take the diameter of the plasma column as 10 cm and the duration as $12 \mu\text{s}$, this gives a total momentum of 2.2 g m/s and a mass of 24 μg . Measurements taken in combination with the interferometer show that the electron density increases by about a factor of 6 when crossing the shock structure upstream of the pressure probe. (See Fig. 18 and compare measurements in Secs. VI B, VI C, and VI E.)

G. Magnetic probes

Several passive magnetic induction probes have been constructed and inserted into the plasma accelerator. These are protected by 3 mm diameter quartz tubes with a half-millimeter thick wall. The probe heads are constructed of magnet wire, with 12–14 turns at a 1 mm nominal diameter. These probes are placed just inside the outer electrode and are aligned to measure the azimuthal component of dB/dt . Two probes are inserted into the main accelerator section, at about the same axial position as the inner electrode's neck. Except for the earliest times, these two probes are strongly correlated with the current. Since the sign of B_ϕ/I is constant, the main current paths are downstream from these probes during most of the shot. In particular, there is no sign of restrikes upstream of this position. From these data, we conclude that the dominant current sheet passes the neck $2\text{--}4 \mu\text{s}$ after the switch closes. Additional magnetic induction probes have been constructed and installed downstream of the inner electrode's nose. These will also be just inside the outer electrode's wall. These have been individually calibrated *in situ* with a $24 \mu\text{s}$ current oscillation. At that frequency, typical sensitivities are about 1×10^{-5} V s/T. These produce waveforms similar to that of the main gun's current

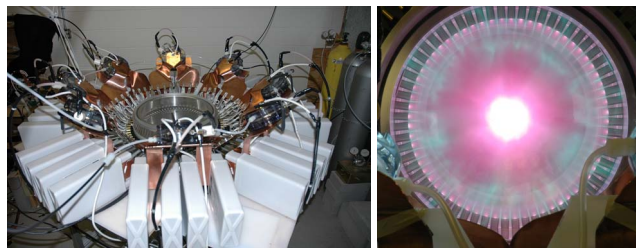


FIG. 22. (Color online) The upgraded TwoPi test fixture has all tungsten electrodes, twice the capacitance per capillary of the original, as well as lower base pressure and better diagnostic access. Test firings exhibit much better symmetry as indicated by Nikon open shutter photograph.

(Sec. VI A), but with much more structure and timedelays dependent on their axial position. From this, we conclude that the dominant current sheet passes the neck in about $3 \mu\text{s}$ and has formed a plasma focus structure by $10 \mu\text{s}$.

H. TwoPi Jet merging and implosion experiments

To examine the physics of the capillaries' coplanar merging jets as they enter the breach of the gun, we utilized the TwoPi test fixture described earlier. Inward radial jet velocity at the nozzles is typically 10–14 km/s as measured by both Doppler shift and photodiodes. Measurements on the TwoPi allow rough descriptions of the plasma fan injected into the gun. An upgraded TwoPi test fixture (Fig. 22) was fabricated with a slightly smaller inner diameter of 12.9 in. (32.8 cm). The height was increased substantially to 15.4 in. (39.1 cm) to allow placement of the large pumpout port on the side, underneath the ring of capillaries. The smaller diameter also allowed the jet nozzles to form a more closely spaced initial ring thus allowing formation of imploding plasma liners. The power supply was upgraded to 0.11 μF per capillary and the ballast resistors were removed to allow more current to the capillaries. The total energy per capillary thus increased from 23 to 67 J. These changes produced the much more energetic plasmas seen in Fig. 22.

Testing with the upgraded TwoPi facility has shown the symmetric implosion of 64 plasma jets to a small central core as shown in Fig. 23. This was produced by what appears to be a precursor shell imploding at roughly 80 km/s but with relatively small mass, and which was then followed tens of microseconds later by the main larger mass shell imploding at a slower 10–14 km/s, Fig. 23. The larger (but slower) mass shell reveals a fairly well defined cylindrical shell which appears to propagate without significant instability to the center, forming another bright core. These tests demonstrate that multiple discrete plasma jets can indeed merge to form imploding plasma shells in a configuration different than that demonstrated earlier by Degnan *et al.*⁴⁴ Further work on this is underway and will be reported in future papers.

The total mass of this imploding shell is estimated to be 100–200 μg . For the MTF application, it is required to have 60 or more large coaxial guns arranged in a spherical array firing toward the center, each of which launches 200 μg , for a total of 12 000 μg of plasma imploding at 200 km/s. Even higher density plasma liners are of interest for PJMIF, so that

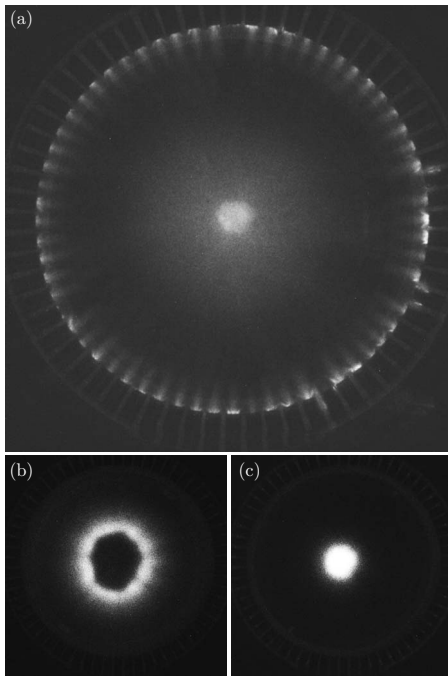


FIG. 23. Well defined imploding plasma liners produced by the merging of 64 discrete plasma jets are observed. (a) A highly symmetric implosion (but with small mass) at 80 km/s produces a small well defined central sphere of higher density plasma (Table I). (b) The slower more massive shell follows much later, and finally collapses in (c). Pictures are contrast enhanced to show detail.

it is important to begin understanding the jet merging and implosion dynamics for such liners produced by multiple merging jets using high- Z gases.

VII. DISCUSSION AND NEXT STEPS

The half-scale prototype gun works roughly as predicted by the MACH2 code in terms of total mass and velocity; but the measured density is lower than desired. In order to attain the full performance potential of these plasma guns, we will need to make upgrades in several key areas. First, we must go to shorter pulse plasma injectors with more mass per pulse. The current approach uses ablating polyethylene capillary discharges as the mass source. Increasing the available current to the discharge and shortening the pulse will provide shorter higher density plasma slugs which should perform better in the subsequent acceleration in the main gun. However, having injected higher mass, we will then need to increase the main drive current by several factors to accelerate the larger mass to even higher velocity. We will need to build PFNs capable of driving about 0.8 MA for 8–10 μ s to achieve full performance. In the case of both injection and main current, shortening the pulse and increasing the current essentially implies going to smaller capacitance operated at higher voltage, which is the direction we are proceeding.

For the pulsed plasma injection, we are investigating several options, which include higher energy capillary discharges, metal-vapor arc discharges, ablative spark discharges, arc-driven plenums with integral burst diaphragm, and minirailgun injectors. The minirailguns appear to hold the most promise because they have the ability to operate

with both ablative capillary mass sources, and more importantly, with pure high density gas using very fast opening valves. Experimental work in this area is progressing rapidly, with preliminary measurements indicating velocities of ~ 60 km/s, electron densities $N_e \sim 10^{17}$ cm $^{-3}$ just outside the muzzle, dropping to $N_e \sim 10^{16}$ cm $^{-3}$ and temperatures $T_e \sim 3$ eV in the jet plume, and rising as high as 7×10^{17} cm $^{-3}$ and 6 eV, respectively, back within the 1 cm square bore minirailgun itself. Further results will be reported in the future.

Lastly, we will need to work with full-scale guns. Such a gun has recently been fabricated and will soon be mounted onto a new much larger vacuum chamber. The old vacuum chamber used to date is far too small to contain the plasma plume of the full-scale gun. The larger vacuum chamber has a diameter of ~ 1 m and is nearly 2 m long, allowing for much higher energy plumes. The new chamber also provides a flight path of sufficient length to diagnose an entire plasma slug in transit. It also will allow simultaneous testing of several full-scale guns so that jet merging experiments at high energy can be performed.

The full-scale gun has been fabricated with a large number of internal probe ports, both azimuthally and axially. This will allow direct local magnetic and spectroscopic measurements to be made in studying the dynamic structure of the plasma armature during acceleration, which has been difficult to do on the smaller scale gun used to date. These measurements will help us confirm whether the blow-by instability is truly being suppressed and if so, under what conditions.

VIII. SUMMARY

A new coaxial plasma accelerator was described which holds promise for eliminating the blow-by instability and allowing attainment of performance beyond that available in present coaxial accelerators. Simulations were described in which blow-by was seen to be avoidable and which attained the ultimate goal of 200 μ g at 200 km/s. Experiments with a first-generation half-scale gun show that the gun performs roughly as designed, although detailed measurements of the magnetic structure deep within the gun still need to be performed. A plan for upgrading the hardware was described for pushing the performance to higher mass, density, and velocity. Considerably more detail regarding experimental results will be forthcoming in papers now in preparation.

ACKNOWLEDGMENTS

The authors are grateful to Dr. Y.C. Francis Thio for originating and encouraging this line of research and to both him and Dr. Jason Cassibry for many useful discussions. The authors are also grateful to Professor Tom York of Ohio State University for his advice on building the fast pressure probe and donation of some essential components. We also gratefully recognize the efforts of David N. van Doren and John Ryan for their expert mechanical/electrical implementations of the plasma jet design, Tim Barrett for design and fabrication of electrical control systems, Brij Barua and Dave van Doren for help with experiment assembly and operation, and to Mike and Sherry Frese of NumerEx for help with MACH2.

This work was supported by the U.S. DOE Office of Fusion Energy Sciences under Grant No. DE-FG02-05ER54810, and SBIR Grants No. DE-FG02-04ER83978 and DE-FG02-05ER84189.

- ¹R. E. Siemon, I. R. Lindemuth, and K. F. Schoenberg, *Comments Plasma Phys. Controlled Fusion* **18**, 363 (1999).
- ²R. E. Siemon, P. J. Turchi, D. C. Barnes, J. H. Degnan, P. Parks, D. Ryutov, and Y. C. F. Thio, Proceedings of the Joint Conference of the 12th International Toki Conference and the 3rd General Scientific Assembly of Asia Plasma and Fusion Association, Toki, Japan, 11–14 December 2001 (unpublished).
- ³I. R. Lindemuth and R. C. Kirkpatrick, *Nucl. Fusion* **23**, 263 (1983).
- ⁴R. C. Kirkpatrick, I. R. Lindemuth, and M. S. Ward, *Fusion Technol.* **27**, 201 (1995).
- ⁵Y. C. F. Thio, E. Panarella, R. C. Kirkpatrick, C. E. Knapp, and F. Wysocki, *Current Trends in International Fusion Research, Proceedings of the 2nd Symposium*, E. Panarella, ed. (NRC Press, National Research Council of Canada, Ottawa, Canada, 1999).
- ⁶Y. C. F. Thio, First U.S. Plasma Jet Workshop, Los Alamos National Laboratory, 24–25 January 2008 (unpublished).
- ⁷S. C. Hsu, *J. Fusion Energy* **28**, 246 (2008).
- ⁸J. Cassibry, S. Thompson, S. Hsu, and D. Witherspoon, *Bull. Am. Phys. Soc.* **53**, 155 (2008).
- ⁹Y. C. F. Thio, C. E. Knapp, R. C. Kirkpatrick, R. E. Siemon, and P. J. Turchi, *J. Fusion Energy* **20**, 1 (2001).
- ¹⁰Y. C. F. Thio, personal communication (September 23, 2003).
- ¹¹K. L. Baker, D. Q. Hwang, R. W. Evans, R. D. Horton, H. S. McLean, S. D. Terry, S. Howard, and C. J. DiCaprio, *Nucl. Fusion* **42**, 94 (2002).
- ¹²K. L. Baker, R. D. Horton, D. Q. Hwang, R. W. Evans, and S. Howard, *IEEE Trans. Plasma Sci.* **30**, 48 (2002).
- ¹³J. T. Cassibry, Y. C. F. Thio, and S. T. Wu, *Phys. Plasmas* **13**, 053101 (2006).
- ¹⁴R. E. Peterkin, M. H. Frese, and C. R. Sovinc, *J. Comput. Phys.* **140**, 148 (1998).
- ¹⁵R. E. Peterkin, Jr. and M. H. Frese, *Air Force Research Laboratory* (Kirkland AFB, NM, 2000).
- ¹⁶R. G. Jahn, *Physics of Electric Propulsion*, 1st ed. (McGraw-Hill, New York, 1968), pp. 272–275, 288–297.
- ¹⁷J. Marshall, *Phys. Fluids* **3**, 134 (1960).
- ¹⁸J. H. Degnan, R. E. Peterkin, Jr., G. P. Baca, J. D. Beason, D. E. Bell, M. E. Dearborn, D. Dietz, M. R. Douglas, S. E. Englert, T. J. Englert, K. E. Hackett, J. H. Holmes, T. W. Hussey, G. F. Kiuttu, F. M. Lehr, G. J. Marklin, B. W. Mullins, D. W. Price, N. F. Roderick, E. L. Ruden, C. R. Sovinec, P. J. Turchi, G. Bird, S. K. Coffey, S. W. Seiler, Y. G. Chen, D. Gale, J. D. Graham, M. Scott, and W. Sommars, *Phys. Fluids B* **5**, 2938 (1993).
- ¹⁹J. H. Hammer, C. W. Hartman, J. L. Eddleman, and H. S. McLean, *Phys. Rev. Lett.* **61**, 2843 (1988).
- ²⁰H. S. McLean, D. Q. Hwang, R. D. Horton, R. W. Evans, S. D. Terry, J. C. Thomas, R. Raman, *Fusion Sci. Technol.* **33**, 252 (1998).
- ²¹M. Rosenbluth, Los Alamos Science and Technology Report No. LA-1850, 1954.
- ²²P. J. Hart, *Phys. Fluids* **5**, 38 (1962).
- ²³Y. C. F. Thio, J. T. Cassibry, and T. E. Markusic, AIAA Joint Propulsion Conference, Indianapolis, IN, Paper AIAA-2002-3803, July 2002 (unpublished).
- ²⁴S. Kohno, Y. Teramoto, I. V. Lisitsyn, S. Katsuki, and H. Akiyama, *IEEE Trans. Plasma Sci.* **27**, 778 (1999).
- ²⁵D. A. Tidman, Y. C. Thio, S. A. Goldstein, and D. S. Spicer, GT-Devices Technical Note No. GTD 86-7, November 1986.
- ²⁶R. L. Burton, S. A. Goldstein, D. A. Tidman, S. Y. Wang, N. K. Winsor, and F. D. Witherspoon, *IEEE Trans. Magn.* **22**, 1410 (1986).
- ²⁷R. L. Burton, D. Fleischer, S. A. Goldstein, and D. A. Tidman, *J. Propul. Power* **6**, 139 (1990).
- ²⁸M. Levin, A. Pukhov, R. F. Hubbard, D. Kaganovich, D. F. Gordon, P. Sprangle, A. Ting, B. Hafizi, and A. Zigler, *Appl. Phys. Lett.* **87**, 261501 (2005).
- ²⁹B. H. P. Broks, W. Van Dijk, J. J. W. van der Mullen, A. J. Gonsalves, T. P. Rowlands-Rees, and S. M. Hooker, *Phys. Plasmas* **14**, 023501 (2007).
- ³⁰D. J. Spence, P. D. S. Burnett, and S. M. Hooker, *Opt. Lett.* **24**, 993 (1999).
- ³¹Y. Ehrlich, C. Cohen, D. Kaganovich, A. Zigler, R. F. Hubbard, P. Sprangle, and E. Esarey, *J. Opt. Soc. Am. B* **15**, 2416 (1998).
- ³²D. J. Spence and S. M. Hooker, *Phys. Rev. E* **63**, 015401(R) (2000).
- ³³C. D. Macchietto, B. R. Benware, and J. J. Rocca, *Opt. Lett.* **24**, 1115 (1999).
- ³⁴B. R. Benware, C. D. Macchietto, C. H. Moreno, and J. J. Rocca, *Phys. Rev. Lett.* **81**, 5804 (1998).
- ³⁵J. J. Rocca, D. P. Clark, J. L. A. Chilla, and V. N. Shlyaptsev, *Phys. Rev. Lett.* **77**, 1476 (1996).
- ³⁶F. D. Witherspoon, R. L. Kincaid, and D. W. Massey, *J. Therm. Spray Technol.* **11**, 119 (2002).
- ³⁷J. T. Cassibry, Ph.D. dissertation, University of Alabama in Huntsville, (2004).
- ³⁸S. P. Lyon and J. D. Johnson, LANL Technical Report No. LA-UR-92-3407, 1992.
- ³⁹D. E. Johnson and D. P. Bauer, *IEEE Trans. Magn.* **25**, 271 (1989).
- ⁴⁰R. H. Lovberg and C. L. Dailey, *AIAA J.* **20**, 971 (1982).
- ⁴¹I. Uzun-Kaymak, S. Messer, R. Bomgardner, A. Case, R. Clary, R. Ellis, R. Elton, C. Teodorescu, F. D. Witherspoon, and W. Young, *Plasma Phys. Controlled Fusion* **51**, 095007 (2009).
- ⁴²P. Mazzotta, G. Mazzitelli, S. Colafrancesco, and N. Vittorio, *Astron. Astrophys. Suppl. Ser.* **133**, 403 (1998).
- ⁴³M. A. Gigoso and V. Cardenoso, *J. Phys. B* **29**, 4795 (1996).
- ⁴⁴J. H. Degnan, W. L. Baker, M. Cowan, Jr., J. D. Graham, J. L. Holmes, E. A. Lopez, D. W. Price, D. Ralph, and N. F. Roderick, *Fusion Technol.* **35**, 354 (1999).